

JGR Space Physics

RESEARCH ARTICLE

10.1029/2020JA028829

Key Points:

- Hemispheric asymmetries of the mid-latitude ionosphere were observed during the first recovery phase of the September 7–8, 2017 storm
- Hemispheric asymmetries were opposite over the European-African and East Asian-Australian sectors simultaneously
- Their formation is likely due to the asymmetries of the thermospheric composition change, vertical plasma drift, and Traveling Ionospheric Disturbance activity

Supporting Information:

Supporting Information may be found in the online version of this article.

Correspondence to:

Z. Wang,
wzihan@umich.edu

Citation:

Wang, Z., Zou, S., Liu, L., Ren, J., & Aa, E. (2021). Hemispheric asymmetries in the mid-latitude ionosphere during the September 7–8, 2017 storm: Multi-instrument observations. *Journal of Geophysical Research: Space Physics*, 126, e2020JA028829. <https://doi.org/10.1029/2020JA028829>

Received 13 OCT 2020
Accepted 15 MAR 2021

© 2021. American Geophysical Union.
All Rights Reserved.

Hemispheric Asymmetries in the Mid-latitude Ionosphere During the September 7–8, 2017 Storm: Multi-instrument Observations

Zihan Wang¹ , Shasha Zou¹ , Lei Liu^{1,2}, Jiaen Ren¹ , and Ercha Aa³ 

¹Department of Climate and Space Sciences and Engineering, University of Michigan, Ann Arbor, MI, USA, ²Ann and H.J. Smead Aerospace Engineering Sciences, University of Colorado, Boulder, CO, USA, ³Haystack Observatory, Massachusetts Institute of Technology, Westford, MA, USA

Abstract Hemispheric asymmetries of the Vertical Total Electron Content (VTEC) were observed during the first recovery phase of the geomagnetic storm on September 7–8, 2017. These asymmetries occurred at the mid latitudes at two different local times simultaneously: In the European-African sector (early morning), the storm time VTEC in the southern/northern hemisphere was higher/lower than the quiet time value, suggesting the southern/northern hemisphere entered the positive/negative phase (N–S+). In the East Asian-Australian sector (afternoon), the storm time VTEC change was positive in the northern hemisphere, but negative in the southern hemisphere (N+S–). The electron density profiles from digisondes demonstrated that the asymmetries appeared in the F region density as well. The plasma drifts data from digisondes, the column-integrated $[O]/[N_2]$ ratio from GUVI onboard the TIMED satellite, and the detrended VTEC were utilized to study the drivers of the asymmetries. Traveling Ionospheric Disturbance (TID) signatures were identified in the digisonde drift and detrended VTEC data before the appearance of the asymmetry. The magnitude of TIDs was larger in the hemisphere where the negative phase occurred later. The storm time $[O]/[N_2]$ ratio change was positive in Africa (S+) and negative in Europe (N–). However, the $[O]/[N_2]$ measurements were not available in the East Asian-Australian sector during the focused period. The hemispheric differences in the vertical drifts were also observed in both sectors. Therefore, the observed hemispheric asymmetries in both sectors are suggested to be due to the hemispheric asymmetries in the thermospheric composition change, vertical drift, and TID activity.

1. Introduction

Ionospheric storms refer to large-scale responses of the ionospheric electron density or Total Electron Content (TEC) during geomagnetic storms. Since the ionosphere is electromagnetically coupled to the solar wind and magnetosphere and collisionally coupled to the thermosphere, the responses of the ionosphere are quite complex during storms. In the mid-latitude region, the electron density/TEC can either increase or decrease during storms, which is referred to as a positive or negative ionospheric storm. Several drivers have been proved to be able to influence the mid-latitude ionosphere directly or indirectly, for example, Joule heating, particle precipitation, penetration electric field, disturbance dynamo electric field, neutral wind, as well as chemical composition (Mendillo, 2006; Pröls, 1995, and references therein). The interplay between these drivers produce different responses and leads to strong spatial and temporal dependence.

The ionospheric responses during storms exhibit strong latitudinal dependence. At high latitudes, the structured external electric field and particle precipitation from the solar wind and magnetosphere mainly control the ionospheric variability. Most times, the ionosphere can respond to these driving forces almost immediately. At the low and mid latitudes, the responses of the ionosphere to the external forces are more complex. The penetration electric field can quickly reach low latitudes after the southward turning of the interplanetary magnetic field (IMF). Later, with the development of the partial ring currents in the night-side equatorial magnetosphere, the Region 2 field-aligned currents (FACs) grow and gradually shield the lowlatitude ionosphere from the penetration electric field (Wolf et al., 2007). The Region 2 FACs connect the partial ring currents to the ionospheric currents. They are downward into the ionosphere in the dusk side and upward out of the ionosphere in the dawn side, opposite to the polarity of the Region 1 FACs at higher latitudes. At the same time, the disturbance winds generated by the external energy deposition at

the high-latitude region travel to the lower latitudes and then create disturbance dynamo electric fields (Lu et al., 2012; Maruyama et al., 2005). The combination of the penetration/shielding and disturbance dynamo electric fields affects the electrodynamics at the low and mid latitudes. The shielding time scale and the traveling time of the equatorward thermospheric disturbance winds are important for understanding the ionospheric responses at the low to mid latitudes during storms, but they are also difficult to obtain based on observations.

Besides the latitudinal dependence, the ionospheric responses during storms are also dependent on local times. G. W. Prölss (1995, and references therein) showed that the positive storms prefer to develop on the dayside, while the negative storms prefer the early morning sector. Assuming that the negative storms are mainly due to the neutral composition change, G. Prölss (1993) explained the local time asymmetry by invoking the fact that it is easier for the meridional disturbance winds to travel to the lower latitudes on the nightside. In addition, the high-latitude energy depositions are not symmetric in local time but are displaced toward the dark hemisphere (G. Prölss, 1980). Maruyama et al. (2005) showed that the contributions from the disturbance dynamo electric field and the penetration electric field are comparable on the nightside, while the latter is more important on the dayside. Mannucci et al. (2009) also showed that the TEC peaks can develop at different local times during different storms and suggested that further studies with comprehensive data are required to understand the local time differences between the neighboring days. Recently, Zhou et al. (2016) found that the TEC increased in the morning sector while decreased in the afternoon sector during the recovery phase of the 2015 St. Patrick's Day storm, and they attributed this surprising observation to a combination of stronger vertical plasma drifts and meridional winds in the morning sector, which lifted the ionosphere in the morning sector. Xiong et al. (2019) focused on the different responses of the Asian and American sectors on September 9–11, 2017, during the late recovery phase. When the American (Asian) sector was on the dayside during 19–20 UT (7–8 UT) on September 11, the ionosphere experienced a negative (positive) storm. They suggested that the diurnal and semidiurnal tidal components contributed to these opposite responses.

Hemispheric asymmetries of the ionospheric responses have also been observed during storms. In general, due to the seasonal thermospheric composition variation, the negative storms are stronger in the summer hemisphere (G. W. Prölss, 1995), while stronger positive storms prefer the winter hemisphere (Goncharenko et al., 2007). Duncan (1969) pointed out that the effect of a storm is to enhance the photochemical mechanism that is dominant for that season. Interestingly, it is found that the hemispheric asymmetry may show opposite trends at different ionospheric layers. Astafyeva, Zakharenkova, and Doornbos (2015) showed that the enhancements of the TEC and the F2 peak density are more prominent in the winter hemisphere, while the topside ionospheric measurements show a larger enhancement in the summer hemisphere, but no change or even decrease in the winter hemisphere.

However, not all storms follow the general seasonal trend. Astafyeva et al. (2020) presented a puzzling case where opposite hemispheric asymmetries occurred during different phases of the August 25, 2018 storm. During the storm main phase, a strong positive TEC storm was observed in the northern (summer) hemisphere, while no storm time deviation in TEC occurred in the southern (winter) hemisphere. The preference of the TEC positive storm for the summer hemisphere is opposite to what earlier studies found for other storms (Goncharenko et al., 2007). Astafyeva et al. (2020) explained this puzzling asymmetry by invoking a combination of weak seasonal thermospheric winds and weak photoionization in the southern hemisphere (winter). During the recovery phase of this storm, the northern (summer) hemisphere experienced a strong negative storm, while no obvious negative storm signatures were observed in the southern hemisphere (winter). This recovery phase asymmetry was similar to other storms and thus was most likely driven by the background seasonal effect combined with the storm time thermospheric composition change.

In another study, Astafyeva, Zakharenkova, and Förster (2015) showed the opposite hemispheric asymmetries of the ionospheric responses in different longitudes (local times) during the main phase and the early recovery phase of the 2015 St. Patrick's Day storm. In the European-African sector, from 08 to 24 UT on March 17 (8–24 LT), stronger positive storm signatures were observed in the northern hemisphere than those in the southern hemisphere. Meanwhile, in the American sector, from 21 UT on March 17 to 05 UT on March 18 (17–01 LT), the southern hemisphere was in the positive phase, while the northern hemisphere was in the negative phase. The authors suggested that the asymmetry in the American sector could be

explained by the hemispheric asymmetry of the thermospheric composition changes as shown in the observations from the TIMED GUVI, while the asymmetry in the European-African sector was more sophisticated. Besides the composition effect, other factors, including the asymmetry in the geomagnetic field and the amplitude and direction of the IMF B_y , may lead to the observed TEC asymmetry in the European-African sector. Later, Yue et al. (2016) also showed that in the Thermosphere-Ionosphere-Electrodynamics General Circulation Model simulations, the Apex geomagnetic fields can generate a stronger asymmetry in the neutral wind and thermospheric composition than the dipole fields. Despite the above studies, the detailed development of the ionospheric hemispheric asymmetry during storms are still not well understood, especially those asymmetries that are opposite to the background seasonal effect.

In this paper, the ionospheric responses were examined during the double-dip storm on September 7–8, 2017. During the first recovery phase, hemispheric asymmetries were found in Vertical Total Electron Content (VTEC) at two different local times simultaneously. In the regions where the VTEC was asymmetric, the electron density profiles (EDPs) from four digisondes were selected to provide the altitude distribution of the electron density, and they confirmed that the F-region density showed similar asymmetries as the VTEC. The plasma drifts from these digisondes, the $[O]/[N_2]$ ratio from GUVI onboard the TIMED satellite, and the detrended VTEC were utilized to study the possible drivers of the asymmetry. Based on our analysis, we suggest that the asymmetries in the neutral composition change, vertical drift, and Traveling Ionospheric Disturbance (TID) activity together generate the hemispheric asymmetries in VTEC and the F-region electron density in each sector.

In Section 2, descriptions of the data set and the data analysis techniques used in this study are shown. In Section 3, the hemispheric asymmetries in the VTEC and the EDP in both sectors are presented. In Section 4, various potential drivers of the observed asymmetries are thoroughly discussed.

2. Data and Analysis Technique

The multi-instrument data set used in this study is described below:

2.1. The Madrigal VTEC

The VTEC is derived from the dual-frequency GNSS measurements. In this work, we used the VTEC data from the Massachusetts Institute of Technology Haystack Observatory Madrigal database (Rideout & Coster, 2006). The spatial resolution of the VTEC is 1° in latitude and 1° in longitude, and the temporal resolution is 5 min.

2.2. Digisonde

Digisondes are digital ionosondes, which use high frequency radio waves for the vertical-incidence remote sounding of the ionosphere. In this study, several products from digisondes were utilized, including the EDP, the plasma drift in vertical and horizontal directions, the F-region peak height (hmF2), and the peak plasma frequency (foF2). They are described in detail below.

2.2.1. Electron Density Profile (EDP)

Digisonde ionograms present signals reflected from the ionosphere in the frequency vs. travel time frame. Radio waves from the ionosonde with frequencies lower than the local ionospheric critical frequency will be reflected below the F region peak, while those with frequencies higher than the critical frequency will not be reflected back. Therefore, ionosondes can detect the bottomside EDP, but cannot provide the topside EDP. Here, with the assumption that the topside ionosphere follows the Chapman function, we use the foF2, hmF2, and the scale height at the F2 peak to specify the topside ionosphere (Huang & Reinisch, 1996).

2.2.2. Plasma Drift

Digisondes can measure the plasma drift based on the echoes reflected by undulated density contours and irregularities (Reinisch et al., 1998). Scali et al. (1995) showed a good agreement between the drifts measured by digisondes and those by Incoherent Scattering Radars (ISRs) at the high latitudes. Bullett (1994)

showed that the digisonde drift technique works best during moderately disturbed nighttime conditions. Note that the drifts measured by digisondes might not be reliable when the production and recombination processes are rapid, for example, near the terminators (Gonzales et al., 1982; Woodman et al., 2006). There can be an artificial downward/upward drift due to the generation/disappearance of the E-layer due to sunrise/sunset. Those artifacts have been carefully avoided in this study.

2.3. Tomography

The ionospheric tomography technique is a powerful tool to reconstruct the 3D structure of the ionospheric electron density. It is a typical inversion problem used to estimate the electron density based on the integrated slant TEC (sTEC) along the line-of-sight of the GNSS satellites and the receivers. In this case, 340 ground-based dual-frequency GNSS receivers in Europe, provided by the EUREF Permanent Network, were used to calculate the GNSS sTEC and the 2D regional VTEC maps. The receiver network is not dense enough in the other sectors to apply the tomography technique. Based on the GNSS sTEC results over the European sector, the state-of-the-art tomography technique (Yao et al., 2020) is applied to resolve the spatial distribution of the electron density. The inversion region is over 35–65°N and 5°W–20°E in the geographic coordinates with the horizontal resolution of 1° in both latitude and longitude. The altitude range of the tomography is from 100 to 1,000 km with varying vertical resolutions, and the resolutions for altitudes below and above 450 km are 10 km and 50 km, respectively. To reconstruct the 3D electron density at time t , the ground-based GNSS sTECs from $t - 20$ min to $t + 20$ min are used, that is, 40 min of GNSS data are used to invert the tomography results at time t . The electron densities from the International Reference Ionosphere-2016 (IRI-2016) model are used as the initial values for the inversion.

2.4. Thermospheric Neutral Density Ratio ($[O]/[N_2]$)

The column-integrated $[O]/[N_2]$ ratio is derived based on the ratio of the 135.6 nm and LBHS emissions measured by GUVI onboard the TIMED satellite (Strickland et al., 1995, 1999, 2004; Zhang et al., 2004). The derived $[O]/[N_2]$ ratio is only available on the dayside. It is a useful parameter to specify the thermospheric composition change, and thus to further infer the thermospheric impact on the ionospheric density production and loss processes. Note that GUVI cannot provide a snapshot of the global thermospheric composition distribution at a given time, instead it needs one day to cover all longitudes. The TIMED satellite was orbiting the 10.7 LT and 22.7 LT plane during this storm.

3. Observations

A double-dip geomagnetic storm occurred on September 7–8, 2017, and has received much attention (Aa et al., 2018, 2019; Habarulema et al., 2020; Imtiaz et al., 2020; Jimoh et al., 2019; Jin et al., 2018; Lei et al., 2018; Mosna et al., 2020; Rout et al., 2019; Shen et al., 2018; Wang et al., 2019; Xiong et al., 2019; Zhang et al., 2019). Figures 1a–1f show the B_y and B_z components of the IMF in the geocentric solar magnetospheric (GSM) coordinates (IMF B_y and B_z), solar wind speed, proton number density, dynamic pressure, and the SYM-H index during September 7–8, 2017. The double-dip storm was driven by multiple interplanetary coronal mass ejections (ICMEs) passing the Earth successively (Shen et al., 2018). The IMF turned southward at around 2040 UT on September 7. At ~2330 UT, a shock-ICME complex structure arrived and the IMF B_z decreased further to below -30 nT. The solar wind speed, proton density, and ram pressure all increased abruptly at the shock arrival. The sudden increase of the SYM-H represented the sudden storm commencement. Then, the SYM-H kept decreasing corresponding to the long-lasting southward IMF and reached the first minimum of -142 nT at ~0100 UT on September 8. The IMF turned northward at ~0230 UT, and the storm began to recover until ~1105 UT. During the first recovery phase (from 0230 UT to 1105 UT), the IMF B_z reversed its direction several times, but most of the time, the IMF was northward. The first recovery phase ceased due to the arrival of another ejecta at ~1105 UT, which led to the second main phase. In this study, we focus on the development of the ionospheric, hemispheric asymmetries during the first recovery phase.

The storm time alterations of the VTEC (dVTEC) from the quiet time values at 04 and 06 UT on September 8 are shown in Figure 2 in the geographic coordinates. The quiet time VTEC on September 7, 2017, was

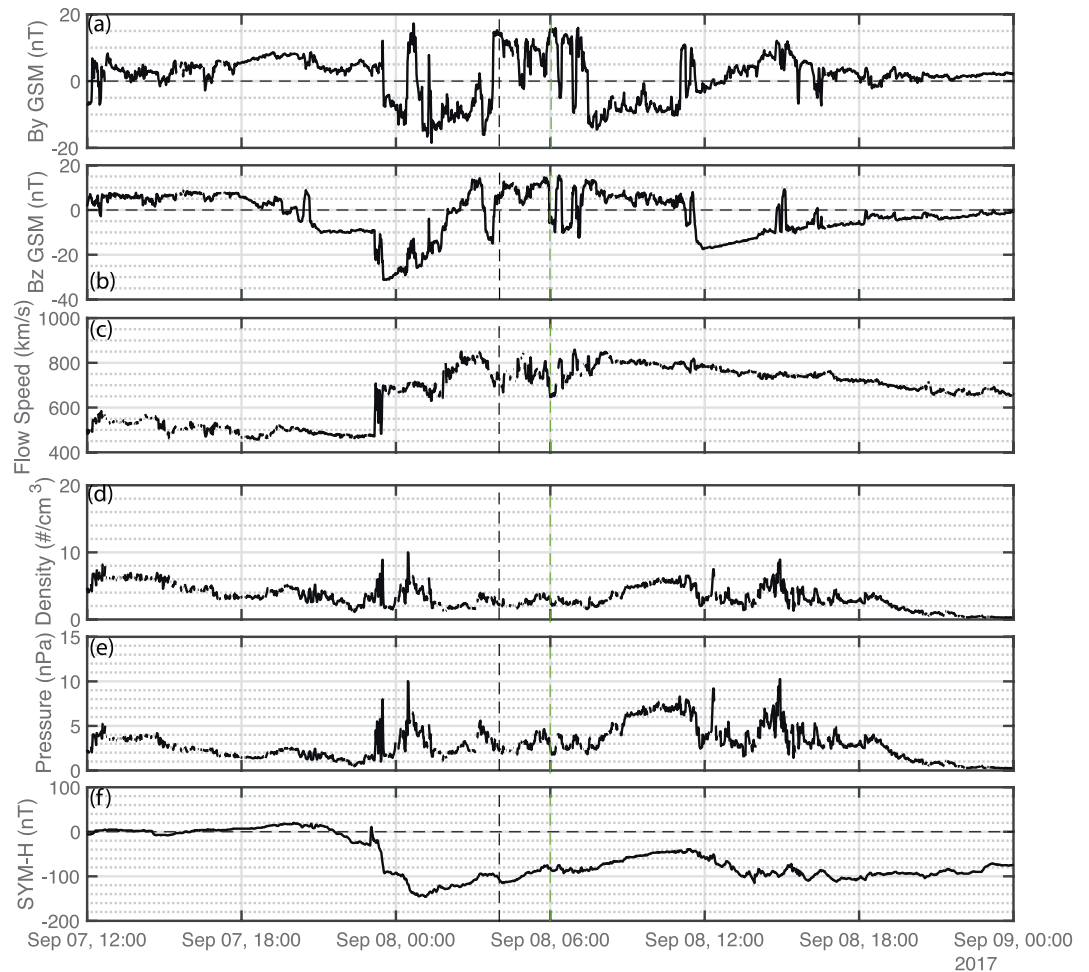


Figure 1. The solar wind data and geomagnetic index from 12 UT September 7 to 0 UT September 9, 2017. (a) IMF By in the GSM coordinates, (b) IMF Bz in the GSM coordinates, (c) solar wind speed, (d) proton number density, (e) solar wind dynamic pressure, and (f) SYM-H index. The black and green vertical lines represent the period that we will focus on later.

removed from the storm time values. The magnetic field lines in the quasi-dipole coordinates at 300 km are plotted on top of the dVTEC map as thin solid lines. The thicker gray line represents the geomagnetic equator. Four digisondes used in this study are also denoted by black stars on the map. A movie of the raw VTEC (left panel) and dVTEC (right panel) is provided as supporting information of this paper, which aims to better visualize where the asymmetries occurred in the context of traditional, large-scale storm time VTEC features. In the movie, it is clear that the large-scale dayside ionosphere was in the positive phase until almost 04 UT on September 8. At this time, the IMF Bz component turned northward, and the SYM-H was gradually recovering. The large-scale ionosphere response began to transit from the positive phase to the negative phase, but the dVTEC was almost hemispherically symmetric. In the East Asian and Australian sector, there were VTEC increases (over 20 TECU) in both hemispheres, which were caused by the widened equatorial ionization anomaly (EIA). In the European and African sector, only minor VTEC increases (~ 5 TECU) were observed in both hemispheres.

Between 04 UT and 06 UT, the IMF remained northward, and the SYM-H recovered to ~ -80 nT. During this period, strong hemispheric asymmetries developed in both the European-African (LT ~ 5 –7) and the East Asian-Australian sectors (LT ~ 12 –16). At 06 UT, these asymmetries became very obvious and they are highlighted by black arrows in Figure 2. Based on the dVTEC movie, these asymmetries developed when the ionosphere transited from the positive phase to the negative phase. In the European-African sector, in the mid-latitude region (20° – 40° MLAT), the VTEC increased in the southern hemisphere, but decreased in the

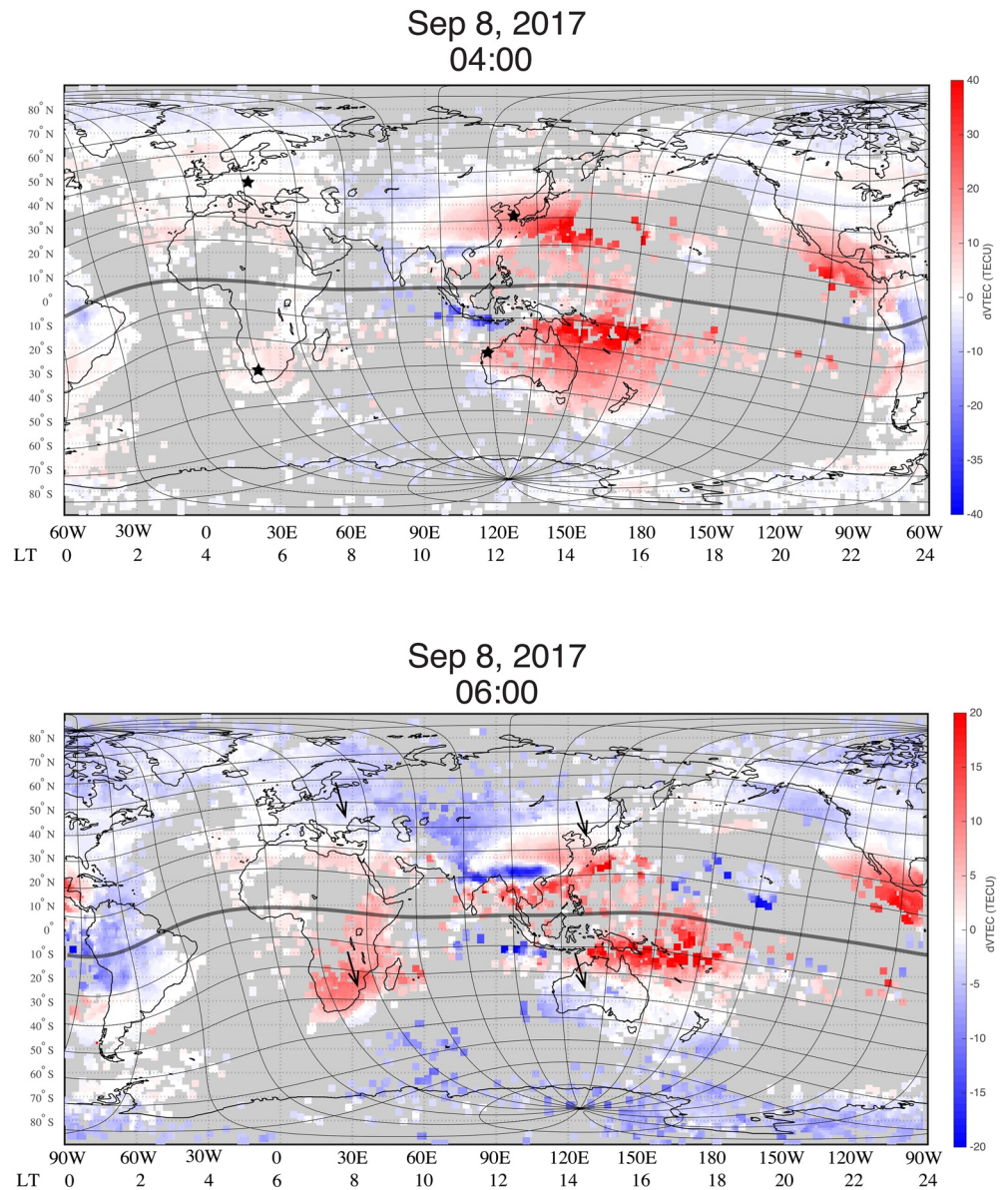


Figure 2. The VTEC difference between September 8, 2017 and September 7 2017. The difference is shown in geographic coordinate with a map of Quasi-Dipole coordinates at 300 km altitude. The asymmetry was highlighted by the black arrows. Four digisondes were represented by stars.

northern hemisphere. The size of the asymmetry was about 15° in longitude and 10° in latitude. This asymmetry was also studied in (Habarulema et al., 2020). On the contrary, in the East Asian-Australian sector around 120°E longitude, the VTEC increased in the northern mid-latitude region ($20^\circ\sim 30^\circ$ MLAT), while decreased in the conjugate southern hemisphere. The size of the asymmetry was larger than the European-Africa sector, which was almost 20° in longitude and 20° in latitude. The time series of the VTEC at four selected locations (labeled as A, B, C, and D), where the asymmetries were observed, are shown in Figure 3. The locations of these four points in the geographic and geomagnetic coordinates are shown in Table 1. The VTEC at each location was the averaged value over a surrounding region of 5° longitude \times 5° latitude to better reflect the regional VTEC changes. The standard deviation of the VTEC values in each surrounding region is plotted as the shaded area together with the averaged values. In the southern hemisphere, Louisvale (B) and Learmonth (D), where digisondes are available, were chosen. Then their geomagnetic conjugate points (A, C) were calculated and selected. Before the shock arrival, the VTECs at the locations A and B

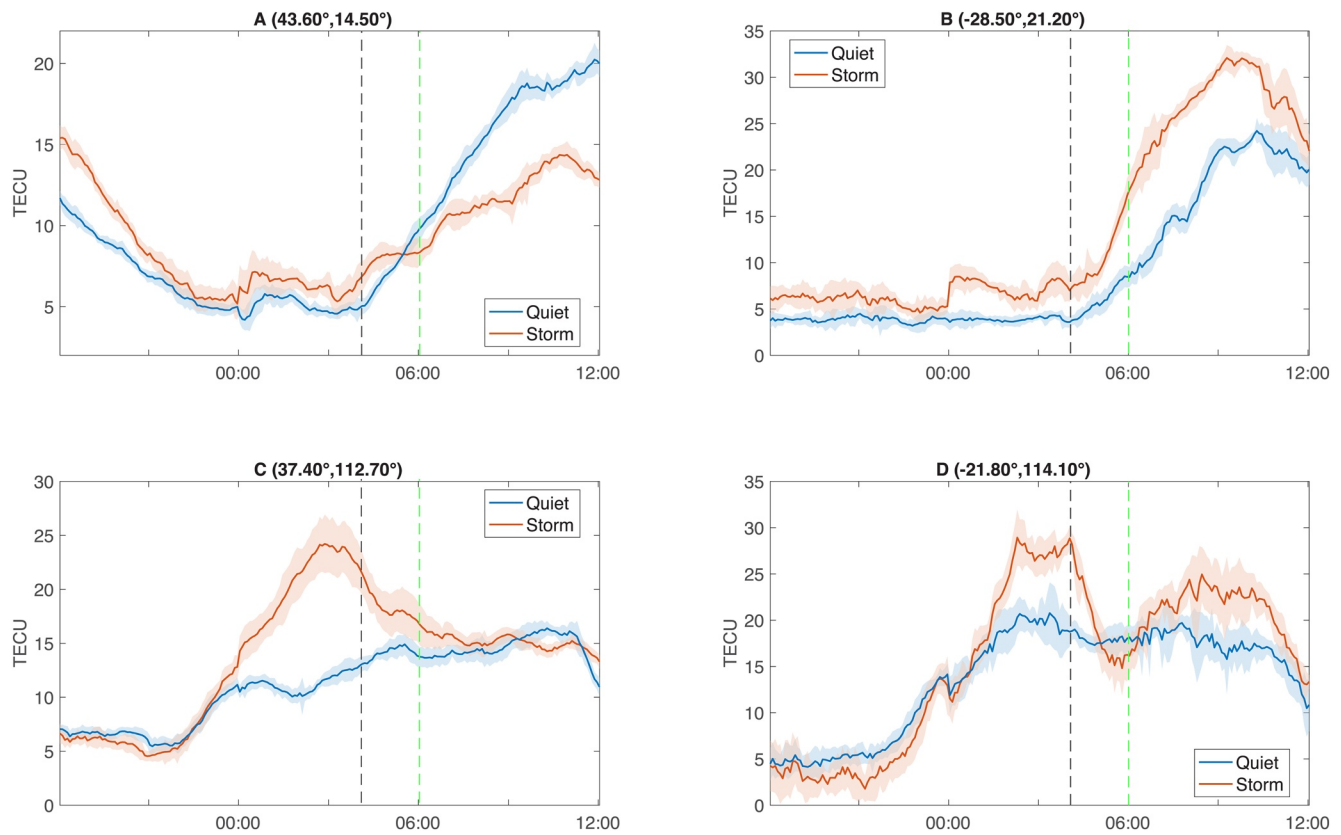


Figure 3. The time series of the VTEC from four locations. The black and green lines represent 04 UT and 06 UT on September 8, respectively. The blue and red lines represent, respectively, the quiet time and storm time values, while the shaded region represents the standard deviation.

were slightly larger than the quiet time values. During the main phase of the storm, the European-African sector was on the nightside and the ionospheric responses to the initial energy input were small with a couple of TECU increase. A large asymmetry began to develop in this sector after 04 UT (sunrise). The VTEC at the location A gradually increased due to sunrise. However, the increasing rate was lower than the quiet time value, resulting in a lower VTEC, i.e., entering the negative phase. On the contrary, the VTEC at the location B increased with a larger rate than the quiet time value, and the $dVTEC$ was always positive with its maximum of 10 TECU at around 10 UT on September 8. Therefore, these two conjugate points in the European-African sector entered the negative and positive phases, respectively, at the same time.

The VTEC at the location C in the East Asian sector and at the location D in the Australian sector began to increase at around 00 UT on September 8, shortly after the shock and strong southward IMF arrival at

Table 1
Geomagnetic Conjugate Locations and the Nearest Digisondes

Location	A	B	C	D
Geographic Latitude	43.6°	-28.5°	37.4°	-21.8°
Geographic Longitude	14.5°	21.2°	112.7°	114.1°
Geomagnetic Latitude	38.0°	-38.0°	32.0°	-32.0°
Nearest Digisonde	Pruhonic	Louisvale	I-Cheon	Learmonth
Geographic Latitude	50.0°	-28.5°	37.1°	-21.8°
Geographic Longitude	14.6°	21.2°	127.5°	114.1°
Geomagnetic Latitude	45.0°	-38.0°	31.0°	-32.0°

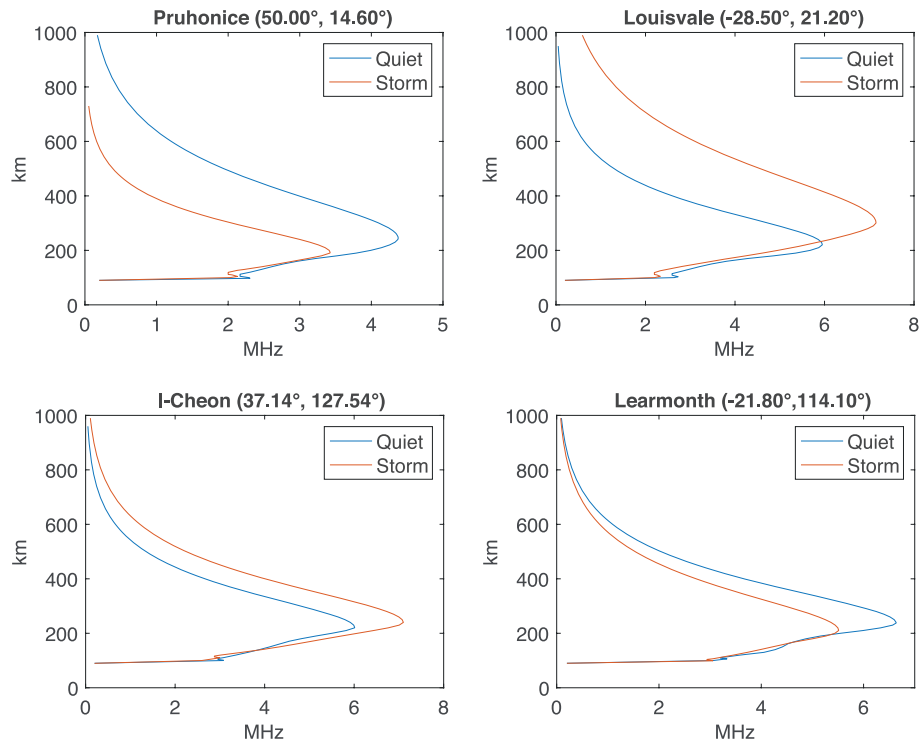


Figure 4. EDP from the four selected digisondes in Figure 2 at 06 UT September 8, 2017. The red curve represents the storm time (September 8) value, while the blue curve represents the quiet time (September 7) value.

the Earth. These increases ceased when the IMF turned northward at around 0230 UT. Later, the VTECs at these two locations started to decrease, but with different speed. The hemispheric asymmetry in VTEC began to develop after 04 UT. The VTEC at the location C gradually decreased and recovered to the quiet time value at around 08 UT. When the VTEC asymmetry was observed at 06 UT, the location C was still in the positive phase. On the other hand, the VTEC at the location D decreased rapidly and became lower than the quiet time value at around 05 UT, that is, entering the negative storm phase. However, this negative storm phase was a short-lived one. The VTEC started to recover and exceeded the quiet time value after 07 UT. Therefore, these two conjugate locations in the East Asian-Australian sector were in the positive and negative phases, respectively. However, the polarity of this asymmetry is opposite to the one observed in the European-African sector.

The four digisondes closest to the four points are selected to provide the EDPs (Figure 4), which help further confirm the existence of the asymmetries at 06 UT. Their locations are also shown in Table 1. Clear asymmetries can be observed in the EDP plots at 06 UT and are consistent with the VTEC observations in Figure 2: At Pruhonice (the closest digisonde to A), the electron density decreased significantly in the F region and the topside ionosphere, while at Louisvale (B), the electron density increased significantly above 250 km, in particular at the F-region peak height. At I-Cheon (the closest digisonde to C), the electron density increased in the whole F region, while at the conjugate Learmonth (D), the electron density decreased in the F region, i.e., opposite to the trend observed in the European-African sector. In the mean time, the hmF2 at Louisvale (B) and I-Cheon (C) increased comparing with that during quiet time, while decreased at Pruhonice (A) and Learmonth (D). Therefore, the VTEC and EDP observations shown in Figures 2–4 clearly demonstrated that hemispheric asymmetries developed during the first recovery phase and were opposite in the East Asian-Australian (N+S–) and European-African (N–S+) sectors. Here N/S indicates the northern/southern hemisphere and +/– indicates positive/negative phase, respectively.

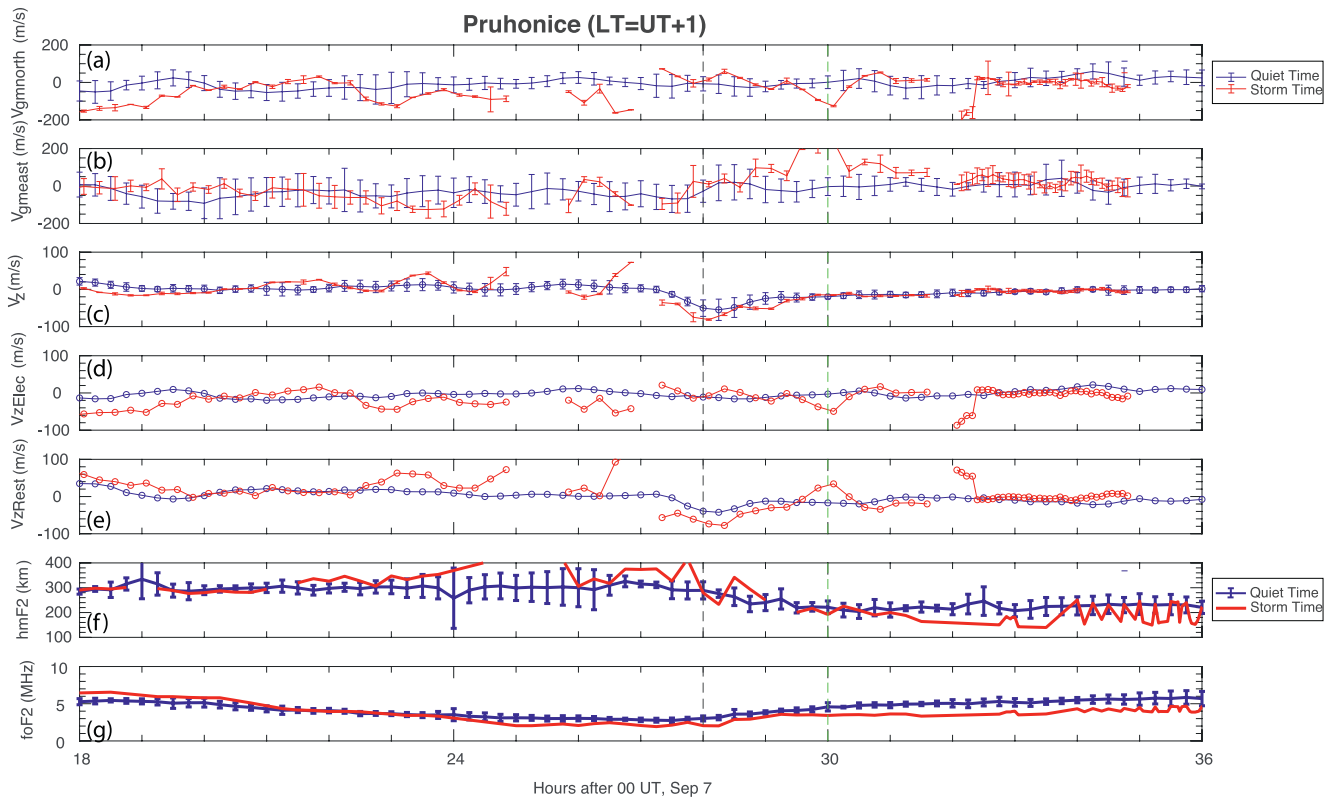


Figure 5. Drift data from the digisonde at Pruhonice. (a) Drift in the geomagnetic north direction. (b) Drift in the geomagnetic east direction. (c) Drift in the vertical direction. (d) Vertical drift due to the electric field. (e) Vertical drift due to the neutral wind and diffusion along the magnetic field line. (f) hmF2. (g) foF2. The black and green lines represent 04 UT and 06 UT, respectively. The red curve represents the storm time (September 7–8) value, while the blue curve represents the quiet time (the average of the previous week) value. The error bars of the quiet time values indicate the quiet time variability, while the error bars of the storm time values represent the uncertainty of the measurements.

4. Discussion

In the mass continuity equation of the ionospheric plasma, the change of the electron density within a certain magnetic flux tube can be due to the vertical plasma drift and the chemical production/loss (Kelley, 2009). The electric field, neutral wind, and ambipolar diffusion along the magnetic field lines can all contribute to the vertical movement of the plasma, and their influences depend on the magnetic field inclination and declination angles (Schunk & Nagy, 2009). The vertical drift can transport the plasma to lower or higher altitudes where the neutral density is higher or lower, and thus affect the plasma lifetime by changing the charge exchange and recombination rates. The upward drift can transport the plasma to higher altitudes, where the charge exchange and recombination rates are lower. Thus, the density at the new F region peak height and topside ionosphere can be larger than that before lifting (Heelis et al., 2009; Zou et al., 2014). If the plasma production is active, the VTEC can increase as well. The thermospheric composition change, on the other hand, can alter the production and loss rates. When the atomic oxygen density ($[O]$) increases in the sunlit region, the production rate will increase, while the increase of the molecular species density (e.g., $[N_2]$) will lead to an enhanced loss rate. Thus, the $[O]/[N_2]$ ratio is a key parameter that can be used to infer the thermospheric composition impact on the TEC (Kil et al., 2011; Mannucci et al., 2009; Strickland et al., 2001; Yue et al., 2016; Zhao et al., 2009). In this section, both the plasma drift and the $[O]/[N_2]$ data are used to study the generation mechanisms of the asymmetries in each sector.

4.1. European and African Sector

The plasma drifts measurements from the digisonde at Pruhonice (A) between 18 UT on September 7 and 12 UT on September 8 are shown in Figure 5. The drifts in the magnetic north, magnetic east, and vertical

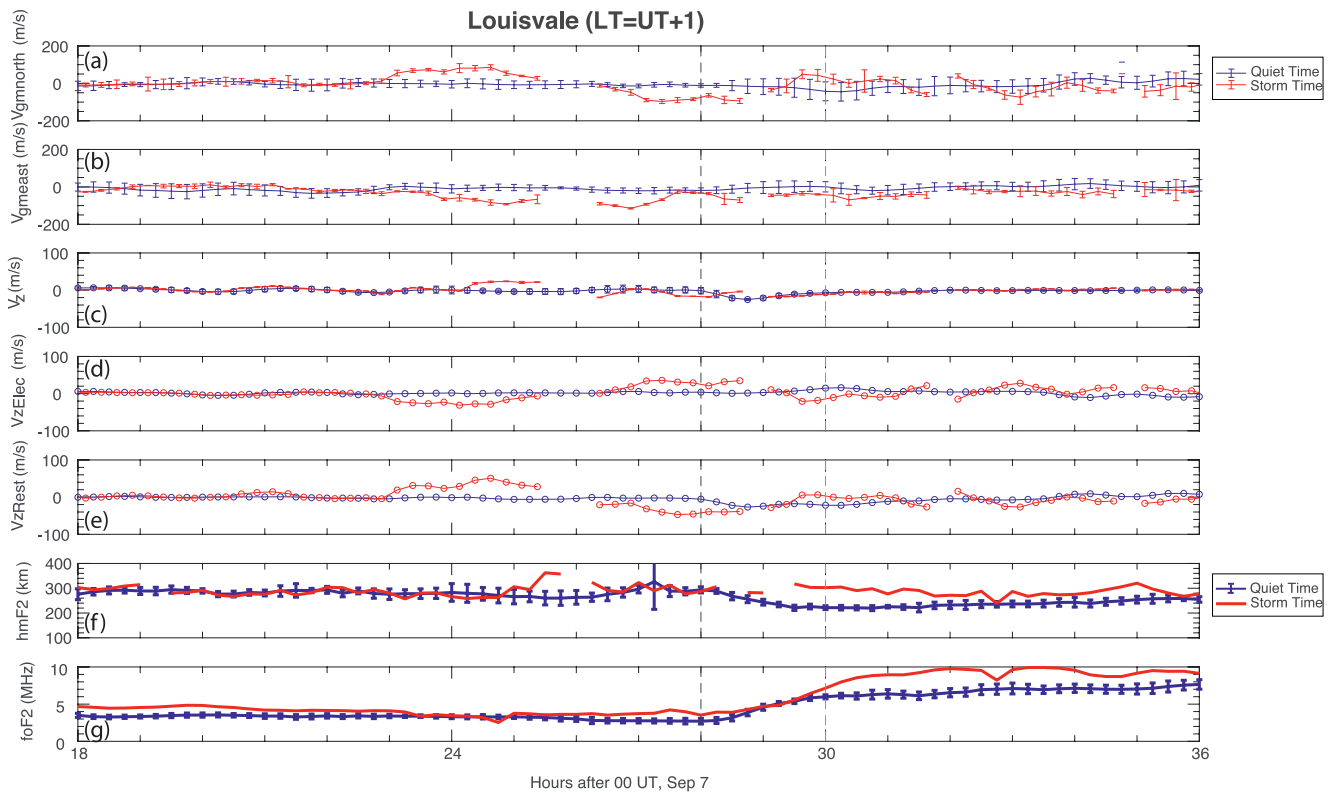


Figure 6. Drift data from the digisonde at Louisvale. The format is the same as Figure 5.

directions are shown in Figures 5a–5c. Schlesier and Buonsanto (1999) and Zou et al. (2013, 2014) separated the contributions to the vertical drift from the electric field, neutral wind, and ambipolar diffusion based on the observations from ISRs. The plasma drift perpendicular to the magnetic field line is due to the electric field, while the drift along the magnetic field line can be attributed to the neutral wind and/or the ambipolar diffusion. A similar method is applied to the digisonde drift measurements in this study. Since the electron and ion temperatures are not available at the locations of these digisondes, the contributions from the neutral wind and the ambipolar diffusion cannot be further separated. In numerical simulations, the contribution from the ambipolar diffusion is usually much smaller than that from the neutral wind (Liu et al., 2016; Lu et al., 2012; Zou & Ridley, 2016). The vertical drift due to the electric field is shown in Figure 5d. The rest of the vertical drift (Figure 5e) is due to the combined effect of neutral wind and diffusion along the magnetic field line. Note that this separation is not applicable near the terminator because of the artificial drift of the digisonde observation described in Section 2.2.2. Figures 5f and 5g show the hmF2 and foF2 measured by digisondes. The red curves represent the storm time values during September 7–8 and the blue curves represent the averaged quiet time values in the previous week. The error bars of the quiet time values indicate the quiet time variability, while the error bars of the storm time values represent the uncertainty of the measurements. The plasma drifts at the other three locations are shown in Figures 6, 10, and 11 in the same format.

The European and African sector was on the nightside during the main phase. Despite sporadic data gaps, the digisonde observations at Pruhonice (A) showed wave-like structures in the vertical drift in Figure 5c. The wave-like structure significantly departed from the quiet time trend and was likely signatures of TIDs. While at Louisvale, the vertical drift oscillated around the quiet time trend with a much smaller amplitude. To further confirm the possible TID signatures and compare their amplitudes in different hemispheres, the keogram of the detrended VTEC over the European-African sector (10°–20°E longitude) from 00 to 06 UT is shown in Figure 7. The detrended VTEC was calculated by subtracting the moving average of the VTEC from the raw VTEC. The sampling window used in this study is 30 min. In the northern hemisphere, there were continuous TIDs propagating from the high-latitude region to the low-latitude region. However, there

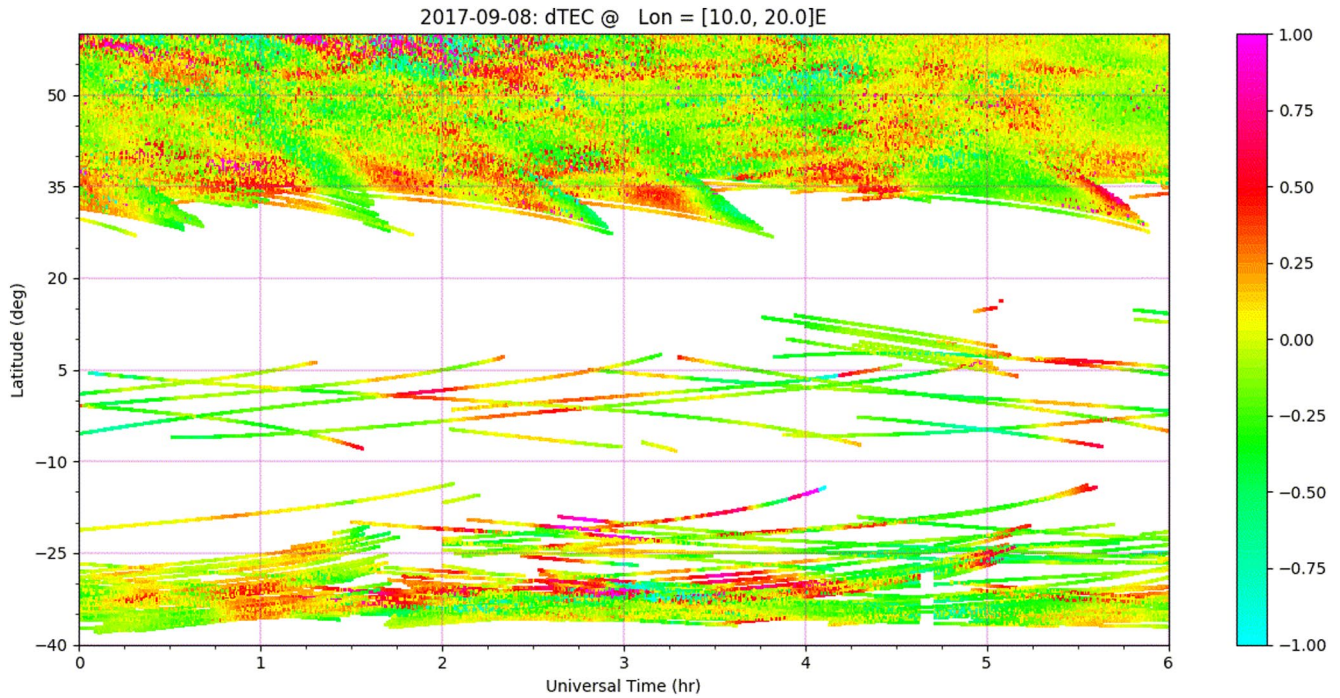


Figure 7. Keogram of the detrended VTEC over the European-African sector.

was limited coverage of the GNSS receivers in the southern hemisphere. Although there were fluctuations in the detrended VTEC in the southern hemisphere, it is hard to compare the amplitude of TIDs in the southern hemisphere with that in the northern hemisphere.

To further evaluate the impact of TIDs in the northern hemisphere, the tomographic inversion results are shown in Figure 8. The left panel shows the EDP at 20°E as a function of latitude and altitude. The poleward boundary of the remnant of the EIA extended to around 48°N. Two electron density islands were located at 55°N and 62°N, respectively. The peaks of these islands were at around 310 km. These two electron islands are likely signatures of the TIDs propagating from the auroral region to the low-latitude region. The right panel shows the EDP at 300 km as a function of longitude and latitude. It shows the impact of TIDs on the

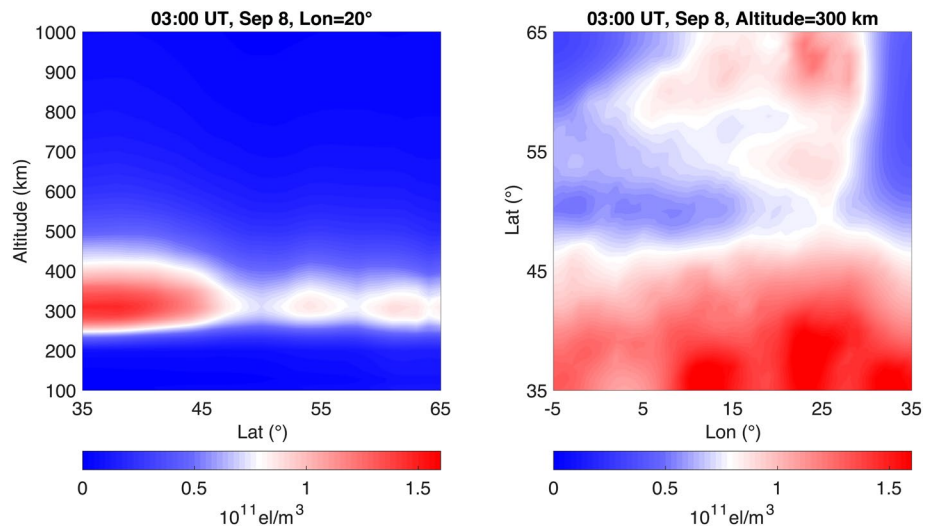


Figure 8. 3D tomography results at 0300 UT, September 8. Left panel: Electron profile at 20°E as a function of latitude and altitude. Right panel: Electron profile at 300 km as a function of longitude and latitude.

electron density from a different view point. Due to the low temporal resolution of the tomographic inversion technique, the propagation of the TID cannot be revealed by this technique. However, the tomographic inversion results, the wave structures observed in the drift data, and the detrended VTEC together strongly suggest the existence of equatorward propagating TIDs in Europe. On the other hand, the TIDs in Africa were less evident due to the limited observations. Based on the drift observation alone, it is likely that the TIDs were weaker in the southern hemisphere in this case. The magnitude of TIDs was larger in the hemisphere where the negative phase occurred later, which suggests there might be a larger energy deposition at the auroral latitudes in the corresponding hemisphere. The hemispheric asymmetry of TIDs observed a couple of hours ahead may signal the development of the asymmetries of VTEC and electron density later during the recovery phase.

As shown in Figures 5d–5e, during the main phase, the electric field at Pruhonice tended to move the plasma downward after the IMF southward turning, while the combined neutral wind and diffusion tended to move the plasma upward and contributed more to the wave-like fluctuations. The net result was that the plasma moved upward, i.e., the hmF2 slightly increased, and thus the VTEC increased as well (Figures 2 and 3). At Louisvale, Figure 6 presented a similar trend in the drift, but with a much smaller amplitude. The hmF2 at Louisvale was close to the quiet time value during this period, with an exception of an hour-long hmF2 increase at about 02 UT. The electric field that led to the plasma descending was likely the penetration electric field on the nightside, while the equatorward meridional winds due to the enhanced heating in the auroral region pushed the plasma along the field line.

The recovery phase of this storm initiated at 0230 UT after the IMF northward turning. In the European sector, at Pruhonice (A) and Louisvale (B), the asymmetry in the vertical drift developed during the early recovery phase. At Pruhonice, there was an enhanced downward movement between 03 and 05 UT, while the drift at Louisvale was always close to the quiet time value during the recovery phase. The downward drift at Pruhonice would move the plasma to lower altitudes with a higher recombination rate, and thus the electron density and VTEC would decrease. The continuous decrease of the hmF2 confirms the expected impact of the downward movement of the ionosphere at Pruhonice. Therefore, the stronger downward drift observed at Pruhonice than that at Louisvale led to the lower VTEC and negative phase as shown in Figure 2, that is, the asymmetry of the plasma drift contributed to the asymmetry of the VTEC.

After sunrise ($LT = UT + 1$ at Pruhonice and Louisvale), due to the solar production, the foF2 at Pruhonice (Figure 5g) started to increase. However, the foF2 was always lower than the quiet time value and the discrepancy continued to increase, which is consistent with the negative phase shown in the VTEC data in Figure 2. On the other hand, the foF2 at Louisvale (Figure 6g) increased faster than the quiet time value after sunrise. Considering it was close to sunrise, chemical production process may also play a role in the formation of the asymmetry. Therefore, the column-integrated $[O]/[N_2]$ ratio data were also studied to evaluate this possibility.

The column-integrated $[O]/[N_2]$ ratio on September 7, September 8 from the TIMED GUVI instrument and their difference are shown in Figure 9 to provide the storm time thermospheric composition change. The orbits of the satellite are plotted on top of the $[O]/[N_2]$ ratio color contours, and the universal times radiolabeled above the top horizontal axis represent when the satellite passed 60°N. The TIMED satellite flew over the European-African sector at 0930 UT, and a clear hemispheric asymmetry in the $[O]/[N_2]$ ratio was observed. The southern edge of Africa was in the region of enhanced $[O]/[N_2]$, while the conjugate Europe was in the region of reduced $[O]/[N_2]$. Note that the VTEC asymmetry occurred at around 0600 UT and lasted until the initiation of the second main phase (Figure 3). Thus, although the composition asymmetry over the European and African sector was measured by GUVI at 0930 UT, it is likely that this asymmetry had already fully developed at 06 UT. As shown in Figure 9, on September 7, the $[O]/[N_2]$ ratio was larger in the southern hemisphere due to the seasonal effect. Then, the storm further enhanced the expected seasonal asymmetry, consistent with earlier studies (Duncan, 1969; Mendillo, 2006).

The effect of the composition change was unmasked by the solar radiation after sunrise. Before sunrise, the molecular species mattered most in the loss process, and no production process existed. However, after sunrise, the production initiated, and the $[O]/[N_2]$ ratio largely determined the electron density and TEC. Besides the TID and vertical drift discussed earlier, we suggest that the difference in the thermospheric

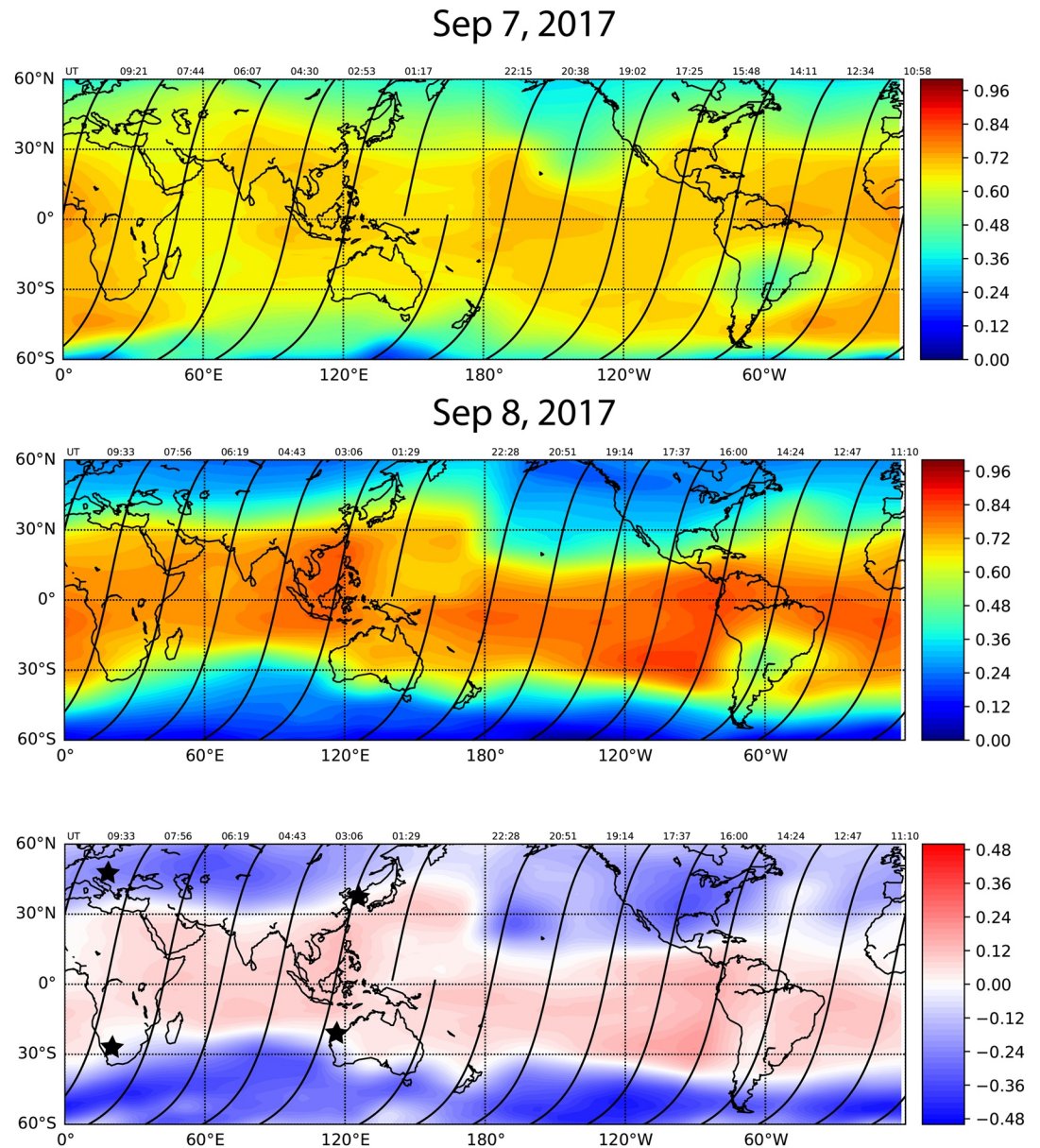


Figure 9. $[O]/[N_2]$ from TIMED GUVI on September 7, September 8 and the difference. The orbits of TIMED are plotted on top of the map. The time represents when the satellite cross 60°N . The satellite is at 10.7/22.7 LT.

chemical composition also contributed to the asymmetry seen both in VTEC and digisonde measurements in the European and African sector.

4.2. East Asian and Australian Sector

During the main phase of this storm, I-Cheon (C) and Learmonth (D) were on the dayside. The equatorial plasma fountain effect amplified on the dayside and led to the widened EIA. A VTEC increase (Figures 2 and 3) was observed in the low-latitude region. I-Cheon and Learmonth were located near the poleward part of the widened EIA. There was no increase of the vertical drift observed at both I-Cheon and Learmonth in Figures 10 and 11 when the shock and strong southward IMF arrived, suggesting that the penetration electric field effect was weak at these two locations. Then, the vertical drift at I-Cheon still followed the quiet time trend except a short drift increase around 1 UT (there were some intermittent data gaps). At the

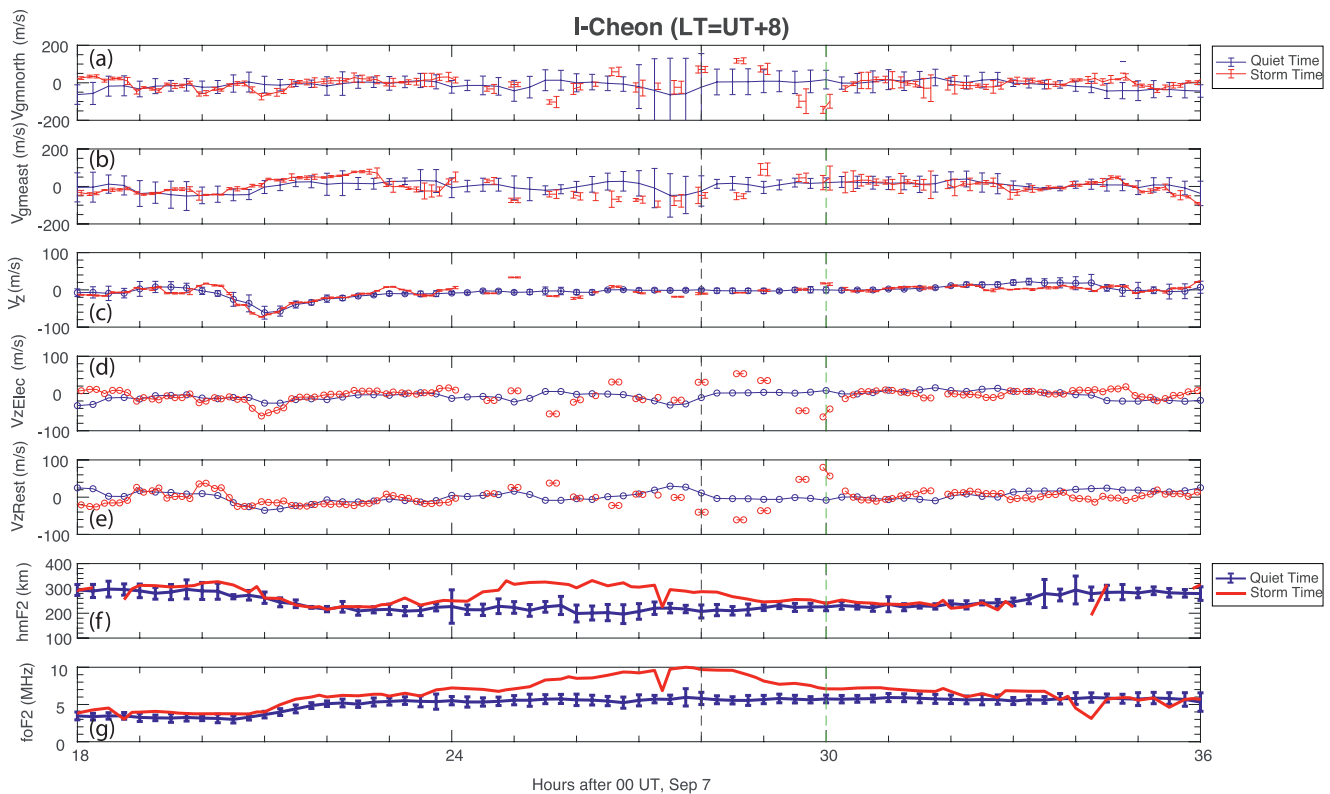


Figure 10. Drift data from the digisonde at I-Cheon. The format is the same as Figure 5.

same time, both the foF2 and hmF2 increased and these enhancements were signatures of the widened EIA. At Learmonth, the vertical drift trend was also similar to the quiet time curve except two local minimums around 01 and 02 UT, respectively. Before 02 UT, the increases of foF2 and hmF2 were also related to the widened EIA. After 02 UT, the hmF2 suddenly began to decrease, which may be related to the northward turning of the IMF.

During 04–06 UT, there were no obvious vertical drifts at I-Cheon and Learmonth. The equatorial electrojet on the same longitude was also close to the quiet time value at this time (Rout et al., 2019). Meanwhile, the hmF2 and foF2 continuously decreased until the asymmetry fully developed at ~06 UT. The faster decreasing rate of the foF2 and hmF2 at Learmonth in the southern hemisphere was likely a result of the downward movement between 02 and 04 UT. This downward movement facilitated an enhanced chemical recombination rate by lowering the plasma to lower altitudes with more molecular neutrals. At 06 UT, both the hmF2 and the foF2 at Learmonth were already lower than the quiet time values, that is, ionospheric negative phase, which is consistent with the short-lived negative phase due to the faster VTEC decrease rate in Figure 3. The differences in the vertical drift between 02 and 04 UT at I-Cheon and Learmonth gave rise to the hemispheric asymmetry in the East Asian and Australian sector. This hints that the history of the storm can play a role in the development of the asymmetry.

Although the total deviation from the quiet time value was small in the vertical drift, the separated contributions from the electric field and the combined neutral wind and diffusion (Figures 10 and 11) presented nontrivial wave-like structures during both the main and recovery phase. Thus, the existence of TIDs was also examined in the East Asian and Australian sector using the detrended VTEC. The keogram of detrended VTEC for the East Asian-Australian sector (120°–130° longitude) from 00 to 06 UT is shown in Figure 12. In both hemispheres, there were continuous TIDs propagating from the polar region to the low-latitude region before 04 UT, and the amplitude of the TIDs was much stronger in the southern hemisphere than that in the conjugate northern hemisphere. The asymmetry of TIDs initiated earlier than the asymmetry of VTEC, which is similar to that seen in the Europe-Africa sector. This suggests the possibility that the energy

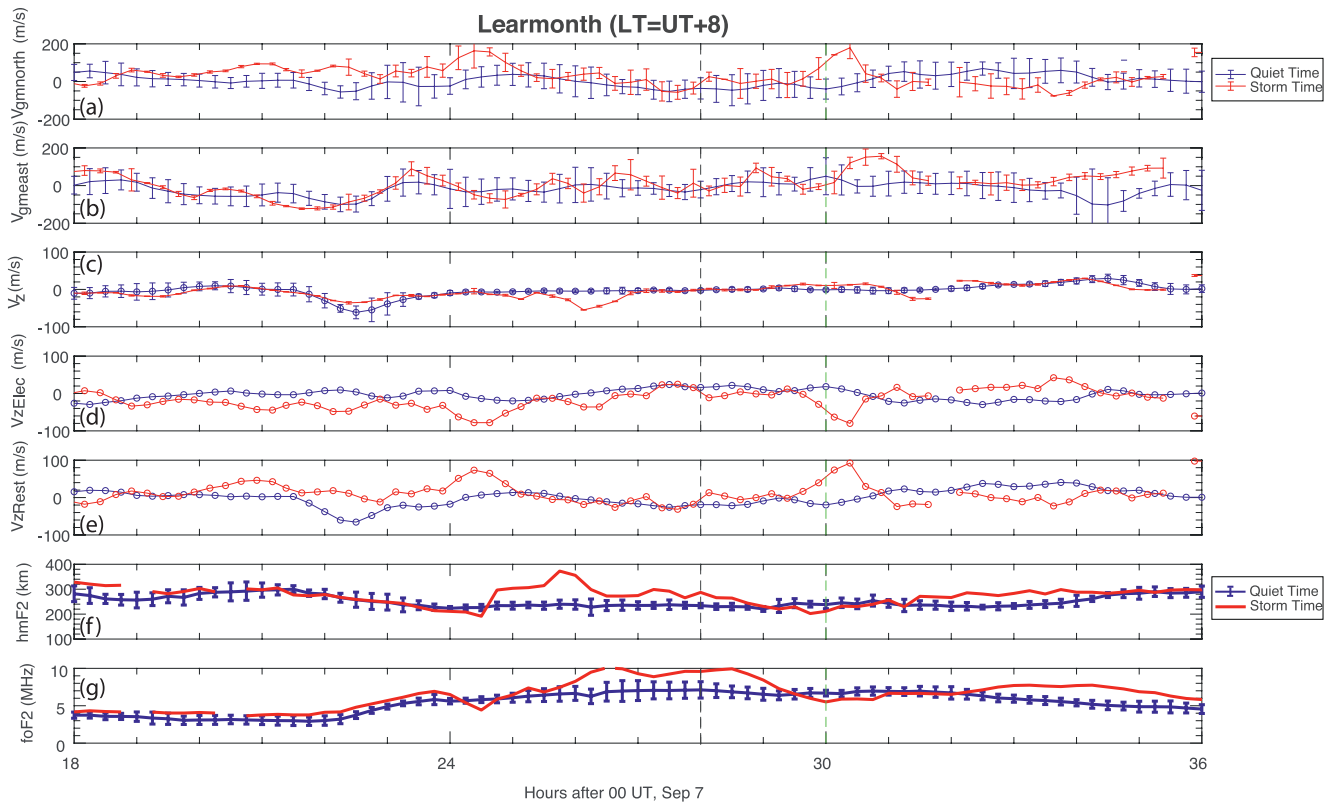


Figure 11. Drift data from the digisonde at Learmonth. The format is the same as Figure 5.

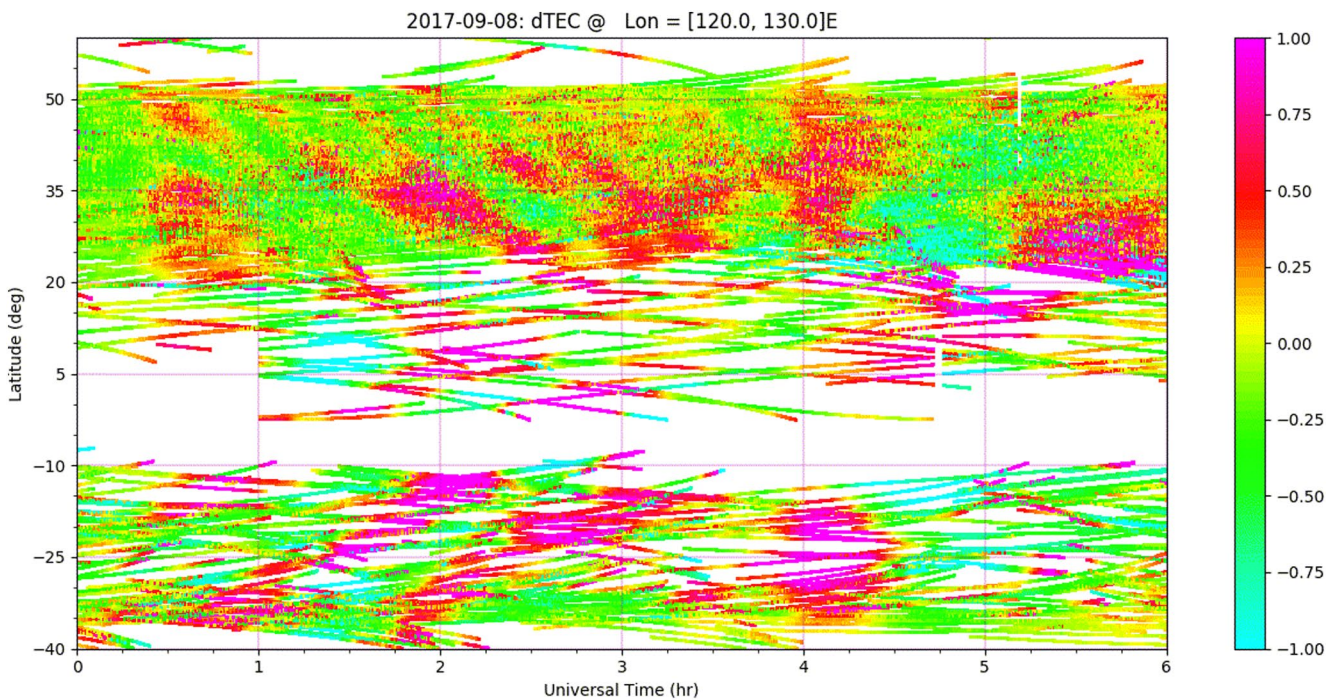


Figure 12. Keogram of the detrended VTEC over the East Asia-Australian sector.

deposition at auroral latitudes was stronger in the southern hemisphere, as inferred from the magnitude of the TIDs, and led to the development of the VTEC asymmetry.

Based on the TID signatures in the drift and dVTEC data, it is found that in both sectors the amplitude of the TIDs was larger in the hemisphere where the negative phase developed later. A further numerical simulation is needed to obtain a more quantitative evaluation.

As shown in Figure 9, at around 03 UT on September 8, the TIMED satellite flew over the East Asian-Australian sector. The $[O]/[N_2]$ ratio increase was similar in both hemispheres at 120°E longitude at this time. No asymmetry in VTEC was observed before 04 UT. During the recovery phase, due to a lack of composition data in this region, it is not possible to determine whether or not the composition changes played a key role in the development of the VTEC asymmetry.

5. Summary and Conclusions

In this study, the ionospheric responses during the first recovery phase of the geomagnetic storm on September 7–8, 2017, were investigated using the GPS VTEC observations, the EDP and plasma drift data from digisondes, and the $[O]/[N_2]$ ratio from TIMED GUVI. Hemispheric asymmetries of the ionospheric responses were observed in the mid-latitude regions at two local times simultaneously. Interestingly, the asymmetries at these two local times were opposite to each other: In the European and African sector (early morning), the southern hemisphere was in the positive phase while the northern hemisphere was in the negative phase, that is, N–S+. In the East Asian and Australian sector (afternoon), the northern hemisphere was in the positive phase and the southern hemisphere was in the negative phase, that is, N+S–, which was opposite to the asymmetry observed in the European and African sector. Hemispheric asymmetries of the vertical plasma drifts were observed in both sectors. In particular, wave-like TID signatures were observed with different magnitudes in different hemispheres. It is also noticed that the magnitude of the TIDs was larger in the hemisphere where the negative storm phase developed later. These TID signatures were further confirmed in the detrended VTEC keogram. The ionospheric tomographic reconstruction using the dense GPS receiver network in Europe revealed the perturbed ionospheric density as a result of the TIDs. In addition, the thermospheric composition inferred from the TIMED GUVI measurements revealed that the storm time $[O]/[N_2]$ change was positive in the Africa region, but negative in the conjugate European region, which suggests that the storm time thermospheric composition change reinforced the seasonal asymmetry and could contribute to the hemispheric asymmetry. Unfortunately, the $[O]/[N_2]$ ratio measurements were not available in the East Asian-Australian sector during the focused period.

In conclusion, the hemispheric asymmetries of the VTEC during this storm recovery phase were generated by a combination of the hemispheric asymmetries of the thermospheric composition change, vertical drift, and TID activity. Some asymmetries of these drivers developed before the appearance of the VTEC asymmetries: The downward drift and stronger TID activity in Europe and Australia likely facilitated the development of the negative phase in the recovery phase. However, it is difficult to quantify the contributions of different drivers based on observations only. A numerical simulation driven by realistic high-latitude drivers is needed for more quantitative evaluations of these various factors that contribute to the observed ionospheric asymmetries.

Data Availability Statement

The GPS TEC data used are available at the Madrigal database (<http://millstonehill.haystack.mit.edu/>). The solar wind, IMF, and Sym-H data are obtained from the NASA Omni web. The digisonde data are available at <http://giro.uml.edu/>. The GUVI data are available at <http://guvitimed.jhuapl.edu/>. The GNSS receiver data are available at <https://www.epncb.oma.be/>.

Acknowledgments

This work is supported by NASA HSR 80NSSC20K1313, NASA LWS 80NSSC20K0190, and FINESST19-HELIO19-0021.

References

Aa, E., Huang, W., Liu, S., Ridley, A., Zou, S., Shi, L., et al. (2018). Midlatitude plasma bubbles over China and adjacent areas during a magnetic storm on 8 September 2017. *Space Weather*, 16(3), 321–331. <https://doi.org/10.1002/2017SW001776>

- Aa, E., Zou, S., Ridley, A., Zhang, S., Coster, A. J., Erickson, P. J., et al. (2019). Merging of storm time midlatitude traveling ionospheric disturbances and equatorial plasma bubbles. *Space Weather*, *17*(2), 285–298. <https://doi.org/10.1029/2018SW002101>
- Astafyeva, E., Bagiya, M. S., Förster, M., & Nishitani, N. (2020). Unprecedented hemispheric asymmetries during a surprise ionospheric storm: A game of drivers. *Journal of Geophysical Research: Space Physics*, *125*, 35–39. <https://doi.org/10.1029/2019JA027261>
- Astafyeva, E., Zakharenkova, I., & Doornbos, E. (2015). Opposite hemispheric asymmetries during the ionospheric storm of 29–31 August 2004. *Journal of Geophysical Research: Space Physics*, *120*(1), 697–714. <https://doi.org/10.1002/2014JA020710>
- Astafyeva, E., Zakharenkova, I., & Förster, M. (2015). Ionospheric response to the 2015 St. Patrick's Day storm: A global multi-instrumental overview. *Journal of Geophysical Research: Space Physics*, *120*(10), 9023–9037. <https://doi.org/10.1002/2015ja021629>
- Bullett, T. W. (1994). *Mid-latitude ionospheric plasma drift: A comparison of digital ionosonde and incoherent scatter radar measurements at Millstone Hill* (Doctoral dissertation). Retrieved from ProQuest Dissertations & theses global. (304103954). University of Massachusetts.
- Duncan, R. A. (1969). F-region seasonal and magnetic-storm behavior. *Journal of Atmospheric and Terrestrial Physics*, *31*(1), 59–70. [https://doi.org/10.1016/0021-9169\(69\)90081-6](https://doi.org/10.1016/0021-9169(69)90081-6)
- Goncharenko, L. P., Foster, J., Coster, A., Huang, C., Aponte, N., & Paxton, L. (2007). Observations of a positive storm phase on September 10, 2005. *Journal of Atmospheric and Solar-Terrestrial Physics*, *69*(10–11), 1253–1272. <https://doi.org/10.1016/j.jastp.2006.09.011>
- Gonzales, C. A., Behnke, R. A., & Woodman, R. F. (1982). Doppler measurements with a digital ionosonde: Technique and comparison of results with incoherent scatter data. *Radio Science*, *17*(5), 1327–1333. <https://doi.org/10.1029/rs017i005p01327>
- Habarulema, J. B., Katamzi-Joseph, Z. T., Bureov, D., Nndanganeni, R., Matamba, T., Tshisaphungo, M., et al. (2020). Ionospheric response at conjugate locations during the 7–8 September 2017 geomagnetic storm over the Europe-African longitude sector. *Journal of Geophysical Research: Space Physics*, *125*(10), e2020JA028307. <https://doi.org/10.1029/2020ja028307>
- Heelis, R. A., Sojka, J. J., David, M., & Schunk, R. W. (2009). Storm time density enhancements in the middle-latitude dayside ionosphere. *Journal of Geophysical Research: Space Physics*, *114*(A3). <https://doi.org/10.1029/2008JA013690>
- Huang, X., & Reinisch, B. W. (1996). Vertical electron density profiles from the digisonde network. *Advances in Space Research*, *18*(6), 121–129. [https://doi.org/10.1016/0273-1177\(95\)00912-4](https://doi.org/10.1016/0273-1177(95)00912-4)
- Imtiaz, N., Younas, W., & Khan, M. (2020). Response of the low- to mid-latitude ionosphere to the geomagnetic storm of September 2017. *Annales Geophysicae*, *38*(2), 359–372. <https://doi.org/10.5194/angeo-38-359-2020>
- Jimoh, O., Lei, J., Zhong, J., Owolabi, C., Luan, X., & Dou, X. (2019). Topside ionospheric conditions during the 7–8 September 2017 geomagnetic storm. *Journal of Geophysical Research: Space Physics*, *124*, 9381–9404. <https://doi.org/10.1029/2019JA026590>
- Jin, H., Zou, S., Chen, G., Yan, C., Zhang, S., & Yang, G. (2018). Formation and evolution of low-latitude F region field-aligned irregularities during the 7–8 September 2017 storm: Hainan Coherent scatter phased array radar and digisonde observations. *Space Weather*, *16*(6), 648–659. <https://doi.org/10.1029/2018SW001865>
- Kelley, M. C. (2009). *The Earth's ionosphere: Plasma physics and electrodynamics*. Academic Press.
- Kil, H., Kwak, Y.-S., Paxton, L. J., Meier, R. R., & Zhang, Y. (2011). O and N2 disturbances in the F region during the 20 November 2003 storm seen from TIMED/GUVI. *Journal of Geophysical Research: Space Physics*, *116*(2). <https://doi.org/10.1029/2010JA016227>
- Lei, J., Huang, F., Chen, X., Zhong, J., Ren, D., Wang, W., et al. (2018). Was magnetic storm the only driver of the long-duration enhancements of daytime total electron content in the Asian-Australian sector between 7 and 12 September 2017? *Journal of Geophysical Research: Space Physics*, *123*(4), 3217–3232. <https://doi.org/10.1029/2017JA025166>
- Liu, J., Wang, W., Burns, A., Solomon, S. C., Zhang, S., Zhang, Y., & Huang, C. (2016). Relative importance of horizontal and vertical transports to the formation of ionospheric storm-enhanced density and polar tongue of ionization. *Journal of Geophysical Research: Space Physics*, *121*(8), 8121–8133. <https://doi.org/10.1002/2016JA022882>
- Lu, G., Goncharenko, L., Nicolls, M. J., Maute, A., Coster, A., & Paxton, L. J. (2012). Ionospheric and thermospheric variations associated with prompt penetration electric fields. *Journal of Geophysical Research: Space Physics*, *117*(8). <https://doi.org/10.1029/2012JA017769>
- Mannucci, A. J., Tsurutani, B. T., Kelley, M. C., Iijima, B. A., & Komjathy, A. (2009). Local time dependence of the prompt ionospheric response for the 7, 9, and 10 November 2004 superstorms. *Journal of Geophysical Research: Space Physics*, *114*(10). <https://doi.org/10.1029/2009JA014043>
- Maruyama, N., Richmond, A. D., Fuller-Rowell, T. J., Codrescu, M. V., Sazykin, S., Toffoletto, F. R., et al. (2005). Interaction between direct penetration and disturbance dynamo electric fields in the storm-time equatorial ionosphere. *Geophysical Research Letters*, *32*(17), 2–5. <https://doi.org/10.1029/2005gl023763>
- Mendillo, M. (2006). Storms in the ionosphere: Patterns and processes for total electron content. *Reviews of Geophysics*, *44*(4), 1–47. <https://doi.org/10.1029/2005RG000193>
- Mosna, Z., Kouba, D., Knizova, P. K., Buresova, D., Chum, J., Sindelarova, T., et al. (2020). Ionospheric storm of September 2017 observed at ionospheric station Pruhonice, the Czech Republic. *Advances in Space Research*, *65*(1), 115–128. <https://doi.org/10.1016/j.asr.2019.09.024>
- Pröls, G. (1993). On explaining the local time variation of ionospheric storm effects. *Annales Geophysicae*, *11*, 1–9.
- Pröls, G. W. (1980). Magnetic storm associated perturbations of the upper atmosphere: Recent results obtained by satellite-borne gas analyzers. *Reviews of Geophysics*, *18*(1), 183–202. <https://doi.org/10.1029/rg018i001p00183>
- Pröls, G. W. (1995). Ionospheric F-region storms. In H. Volland, (Ed.), *Handbook of atmospheric electrodynamics (1995)* (Vol. II, (pp. 195–235). CRC Press.
- Reinisch, B. W., Scali, L., & Haines, D. M. (1998). Ionospheric Drift measurements with digisondes (Vol. 41). *Annali Di Geofisica*.
- Rideout, W., & Coster, A. (2006). Automated gps processing for global total electron content data. *GPS Solutions*, *10*(3), 219–228. <https://doi.org/10.1007/s10291-006-0029-5>
- Rout, D., Pandey, K., Chakrabarty, D., Sekar, R., & Lu, X. (2019). Significant electric field perturbations in low latitude ionosphere due to the passage of two consecutive ICMEs during 6–8 September 2017. *Journal of Geophysical Research: Space Physics*, *124*(11), 9494–9510. <https://doi.org/10.1029/2019JA027133>
- Scali, J. L., Reinisch, B. W., Heinselman, C. J., & Bullett, T. W. (1995). Coordinated digisonde and incoherent scatter radar F region drift measurements at Sondre Stromfjord. *Radio Science*, *30*(5), 1481–1498. <https://doi.org/10.1029/95rs01730>
- Schlesier, A. C., & Buonsanto, M. J. (1999). The Millstone Hill ionospheric model and its application to the May 26–27, 1990, ionospheric storm. *Journal of Geophysical Research: Space Physics*, *104*(A10), 22453–22468. <https://doi.org/10.1029/1999ja900250>
- Schunk, R., & Nagy, A. (2009). *Ionospheres: Physics, plasma physics, and chemistry*. Cambridge University Press.
- Shen, C., Xu, M., Wang, Y., Chi, Y., & Luo, B. (2018). Why the shock-ICME complex structure is important: learning from the early 2017 September CMEs. *The Astrophysical Journal*, *861*(1), 28. <https://doi.org/10.3847/1538-4357/aac204>
- Strickland, D., Meier, R., Walterscheid, R., Craven, J., Christensen, A., Paxton, L., et al. (2004). Quiet-time seasonal behavior of the thermosphere seen in the far ultraviolet dayglow. *Journal of Geophysical Research: Space Physics*, *109*(A1). <https://doi.org/10.1029/2003ja010220>

- Strickland, D. J., Bishop, J., Evans, J. S., Majeed, T., Shen, P. M., Cox, R. J., et al. (1999). Atmospheric ultraviolet radiance integrated code (AURIC): Theory, software architecture, inputs, and selected results. *Journal of Quantitative Spectroscopy and Radiative Transfer*, 62(6), 689–742. [https://doi.org/10.1016/s0022-4073\(98\)00098-3](https://doi.org/10.1016/s0022-4073(98)00098-3)
- Strickland, D. J., Daniell, R. E., & Craven, J. D. (2001). Negative ionospheric storm coincident with DE 1-observed thermospheric disturbance on October 14, 1981. *Journal of Geophysical Research*, 106(A10), 21049–21062. <https://doi.org/10.1029/2000JA000209>
- Strickland, D. J., Evans, J. S., & Paxton, L. J. (1995). Satellite remote sensing of thermospheric O/N2 and solar EUV: 1. Theory. *Journal of Geophysical Research*, 100(A7), 12217–12226. <https://doi.org/10.1029/95ja00574>
- Wang, Z., Zou, S., Coppeans, T., Ren, J., Ridley, A., & Gombosi, T. (2019). Segmentation of SED by boundary flows associated with Westward drifting partial ring current. *Geophysical Research Letters*, 46(14), 7920–7928. <https://doi.org/10.1029/2019GL084041>
- Wolf, R. A., Spiro, R. W., Sazykin, S., & Toffoletto, F. R. (2007). How the Earth's inner magnetosphere works: An evolving picture. *Journal of Atmospheric and Solar-Terrestrial Physics*, 69(3), 288–302. <https://doi.org/10.1016/j.jastp.2006.07.026>
- Woodman, R. F., Chau, J. L., & Ilma, R. R. (2006). Comparison of ionosonde and incoherent scatter drift measurements at the magnetic equator. *Geophysical Research Letters*, 33(1). <https://doi.org/10.1029/2005GL023692>
- Xiong, C., Lühr, H., & Yamazaki, Y. (2019). An opposite response of the low-latitude ionosphere at Asian and American sectors during storm recovery phases: Drivers from below or above. *Journal of Geophysical Research: Space Physics*, 124(7), 6266–6280. <https://doi.org/10.1029/2019JA026917>
- Yao, Y., Zhai, C., Kong, J., Zhao, C., Luo, Y., & Liu, L. (2020). An improved constrained simultaneous iterative reconstruction technique for ionospheric tomography. *GPS Solutions*, 24, 1–19. <https://doi.org/10.1007/s10291-020-00981-4>
- Yue, X., Wang, W., Lei, J., Burns, A., Zhang, Y., Wan, W., et al. (2016). Long-lasting negative ionospheric storm effects in low and middle latitudes during the recovery phase of the 17 March 2013 geomagnetic storm. *Journal of Geophysical Research: Space Physics*, 121(9), 9234–9249. <https://doi.org/10.1002/2016JA022984>
- Zhang, S. R., Erickson, P. J., Coster, A. J., Rideout, W., Vierinen, J., Jonah, O., & Goncharenko, L. P. (2019). Subauroral and polar traveling ionospheric disturbances during the 7–9 September 2017 Storms. *Space Weather*, 17(12), 1748–1764. <https://doi.org/10.1029/2019SW002325>
- Zhang, Y., Paxton, L. J., Morrison, D., Wolven, B., Kil, H., Meng, C. I., et al. (2004). O/N2 changes during 1–4 October 2002 storms: IMAGE SI-13 and TIMED/GUVI observations. *Journal of Geophysical Research*, 109(A10). <https://doi.org/10.1029/2004JA010441>
- Zhao, B., Wan, W., Liu, L., Igarashi, K., Yumoto, K., & Ning, B. (2009). Ionospheric response to the geomagnetic storm on 13–17 April 2006 in the West Pacific region. *Journal of Atmospheric and Solar-Terrestrial Physics*, 71(1), 88–100. <https://doi.org/10.1016/j.jastp.2008.09.029>
- Zhou, Y. L., Lühr, H., Xiong, C., & Pfaff, R. F. (2016). Ionospheric storm effects and equatorial plasma irregularities during the 17–18 March 2015 event. *Journal of Geophysical Research: Space Physics*, 121(9), 9146–9163. <https://doi.org/10.1002/2016JA023122>
- Zou, S., Moldwin, M. B., Ridley, A. J., Nicolls, M. J., Coster, A. J., Thomas, E. G., & Ruohoniemi, J. M. (2014). On the generation/decay of the storm-enhanced density plumes: Role of the convection flow and field-aligned ion flow. *Journal of Geophysical Research: Space Physics*, 119(2005), 8543–8559. <https://doi.org/10.1002/2014JA019887>
- Zou, S., & Ridley, A. J. (2016). Modeling of the evolution of storm-enhanced density plume during the 24 to 25 October 2011 geomagnetic storm. In C. Chappell, R. Schunk, P. Banks, J. Burch, & R. Thorne (Eds.), *Magnetosphere-ionosphere coupling in the solar system* (pp. 205–213). John Wiley & Sons, Inc. <https://doi.org/10.1002/9781119066880.ch16>
- Zou, S., Ridley, A. J., Moldwin, M. B., Nicolls, M. J., Coster, A. J., Thomas, E. G., & Ruohoniemi, J. M. (2013). Multi-instrument observations of SED during 24–25 October 2011 storm: Implications for SED formation processes. *Journal of Geophysical Research: Space Physics*, 118(12), 7798–7809. <https://doi.org/10.1002/2013JA018860>